





On the Energy Conversion Rate during Collisionless Magnetic Reconnection

Yongyuan Yi^{1,2} , Meng Zhou^{1,2,3}, Liangjin Song^{1,2} , and Xiaohua Deng²

¹Department of Physics, School of Sciences, Nanchang University, Nanchang 330031, People's Republic of China

²Institute of Space Science and Technology, Nanchang University, Nanchang 330031, People's Republic of China

Received 2019 August 3; revised 2019 August 27; accepted 2019 August 30; published 2019 September 23

Abstract

Magnetic reconnection efficiently converts magnetic energy into kinetic and thermal energy of plasmas. The electric field at the X-line, which represents the reconnection rate, is commonly used to measure how fast the reconnection proceeds. However, the energy conversion rate (ECR) has rarely been investigated. Using a 2.5D particle-in-cell simulation, we have examined the temporal evolution of the ECR in collisionless reconnection. It is found that the ECR reaches peak significantly later than the reconnection rate does. This is because the energy conversion primarily occurs at the reconnection fronts rather than at the X-line. With the increase of the inflow density, both the reconnection rate and the conversion rate decrease. The presence of a guide field leads to the reduction of both the reconnection rate and the conversion rate, though reconnection remains fast. We further find that ECR does not depend on the mass ratio but is sensitive to the length of the simulation domain.

Unified Astronomy Thesaurus concepts: [Solar magnetic reconnection \(1504\)](#); [Plasma physics \(2089\)](#); [Space plasmas \(1544\)](#); [Astronomical simulations \(1857\)](#)

1. Introduction

Magnetic reconnection is widely believed to be the main cause of many eruptive phenomena in our solar-terrestrial system (e.g., Russell & McPherron 1973; Chen & Shibata 2000; Deng & Matsumoto 2001; Zhou et al. 2017a). Magnetic energy is rapidly transferred to the kinetic and thermal energy of plasmas during the reconfiguration of magnetic fields. Magnetic topology change and energy conversion are the two fundamental features of magnetic reconnection.

Reconnection rate, defined as the rate of magnetic flux change through the reconnecting current sheet, is commonly used to measure how fast the reconnection proceeds. The Sweet–Parker model (Parker 1957; Sweet 1958) predicts a reconnection rate that is too slow to explain the rapid release of magnetic energy observed in space. The Petschek model (Petschek 1964) obtains a faster reconnection rate than the Sweet–Parker model; however, it requires a localized resistivity, the mechanism of which is unclear. When the resistivity is uniform, it degenerates to Sweet–Parker reconnection (Biskamp 1986; Kulsrud 2001).

The Hall reconnection model, which was developed about one decade ago, suggests that the Hall effect is the key physics for fast reconnection widely observed in space. The main idea is that reconnection rate is controlled by the dynamics of dispersive waves (e.g., whistler or kinetic Alfvén waves) at length scales much greater than the electron dissipation region and is independent of the mechanism breaking the electron frozen-in condition (Shay et al. 1999; Birn et al. 2001; Pritchett 2001). Thus, reconnection rate is constrained by the aspect ratio of the ion dissipation region, which is the ratio of the thickness to the length of the ion dissipation region, and can be much faster than that in the Sweet–Parker model. It is interesting that there is a universal normalized reconnection rate of ~ 0.1 for quasi-steady reconnection in different plasma systems (Shay & Drake 1998; Shay et al. 1999; Liu et al. 2015, 2017). Liu et al. (2017) propose that the reconnection

rate is constrained by the macroscopic boundary condition instead of the microphysics within the microscopic diffusion region.

Recent satellite observations and numerical simulations found that energy conversion not only occurs at the X-line, but also in the outflow region where the magnetic flux pileup occurs (Lapenta et al. 2014; Sitnov et al. 2014; Huang et al. 2015). Khotyaintsev et al. (2016) demonstrated that the motional electric field E_y and ion current J_{iy} led to strong energy conversion at the dipolarization front. In laboratory reconnection, it is found that nearly half of the magnetic energy is converted to plasma, two-thirds of which is converted to ions and one-third to electrons (Yamada et al. 2014). Recently, Lu et al. (2019) found that larger cross-sheet density and temperature inhomogeneities leads to a higher energy conversion rate (ECR).

The lack of systematic investigation of the ECR impedes the comprehensive understanding of fast reconnection. In this paper, we study the ECR by performing a series of 2.5D particle-in-cell (PIC) simulation. According to Poynting theorem, the temporal change of magnetic energy $\partial(B^2/2\mu_0)/\partial t$ equals the divergence of Poynting flux $(-1/\mu_0)\nabla \cdot (E \times B)$ plus the ohmic heating $J \cdot E$. Considering a closed system (or a system with periodic boundaries), the integration of Poynting flux in the entire system disappears, thus the overall ECR equals the spatial integration of $J \cdot E$ over the entire system. For convenience, the ECR mentioned in this paper refers to the overall ECR. Here we examine the temporal evolution of the ECR and the dependence of ECR on the initial parameters of the simulation, such as the inflow density, guide field strength, and mass ratio.

2. Simulation Model

We employed a 2.5D PIC fully electromagnetic code that has been used to study magnetic island and separatrix dynamics associated with magnetic reconnection (Zhou et al. 2011, 2012a, 2012b, 2014; Huang et al. 2014). More details about this PIC code can be found in Zhou et al. (2012a).

³ monmomentum82@gmail.com

Table 1
The Parameters of Each Simulation

Case	$L_x \times L_z$	m_i/m_e	n_b/n_0	d_i	B_{y0}	c/v_A
1	$120d_i \times 60d_i$	100	0.1	40	0	20
2	$60d_i \times 60d_i$	100	0.04	40	0	20
3	$60d_i \times 60d_i$	100	0.2	40	0	20
4	$60d_i \times 60d_i$	100	0.6	40	0	20
5	$60d_i \times 60d_i$	100	1	40	0	20
6	$60d_i \times 60d_i$	100	0.2	40	0.5	20
7	$60d_i \times 60d_i$	100	0.2	40	1	20
8	$60d_i \times 60d_i$	100	0.2	40	2	20
9	$60d_i \times 60d_i$	25	0.2	20	0	15
10	$60d_i \times 60d_i$	400	0.2	80	0	40
11	$60d_i \times 120d_i$	100	0.2	40	0	20
12	$120d_i \times 60d_i$	100	0.2	40	0	20

Note. The fifth column indicates the number of grids representing one d_i .

Periodic boundary conditions are applied in both the X and Z directions. In the Y direction, we set $\partial/\partial y = 0$, that is, no spatial variation along the Y direction.

The initial equilibrium configuration is given by two Harris current sheets

$$B_x = B_0 \tanh((z - L_z/4)/L_0) - B_0 \tanh((z - 3L_z/4)/L_0) - B_0,$$

where B_0 is the asymptotic magnetic field, L_z is the length of simulation region in the Z direction, and L_0 is the initial half-width of the current sheet. The initial ion and electron temperature are uniform; hence plasma density is varied across the current sheet to maintain pressure balance along the Z direction. For convenience, we present the simulation results from the upper current sheet only.

In order to understand how the ECR varies with the initial parameters, we have performed a series of simulations with different inflow plasma densities $n_b/n_0 = 0.04, 0.2, 0.6, 1$, different guide fields $B_{y0} = 0, 0.5, 1, 2$, and different mass ratios $m_i/m_e = 25, 100, 400$. Here n_b is the background plasma density and n_0 is the plasma density in the current sheet center in Harris equilibrium. The detailed parameters for each simulation are listed in Table 1. The inflow density is set by specifying the background plasma density in the simulation, which is uniform in the simulation region. Because the density is zero in the inflow region further away from the neutral sheet in Harris equilibrium, the background density n_b represents the plasma density in the inflow region.

All the results are presented in normalized units. The magnetic field is normalized by B_0 . The density is normalized by the density at the current sheet center n_0 . The velocities are normalized by the Alfvén speed $v_A = B_0/(4\pi n_0 m_i)^{1/2}$. The electric field is normalized by $B_0 v_A$. Lengths are normalized by the ion inertial length in the central current sheet $d_i = c/\omega_{pi} = c/(n_0 q^2/m_i \epsilon_0)^{1/2}$. Time is normalized by the inverse ion cyclotron frequency $\Omega_i^{-1} = m_i/qB$ and the ECR is normalized by $qn_0 v_A^2 B_0 d_i^2$.

3. Results

3.1. The Relationship between ECR and the Reconnection Rate

Figure 1 presents the time evolutions of the reconnection rate and the ECR in case 1. The reconnection rate is defined as

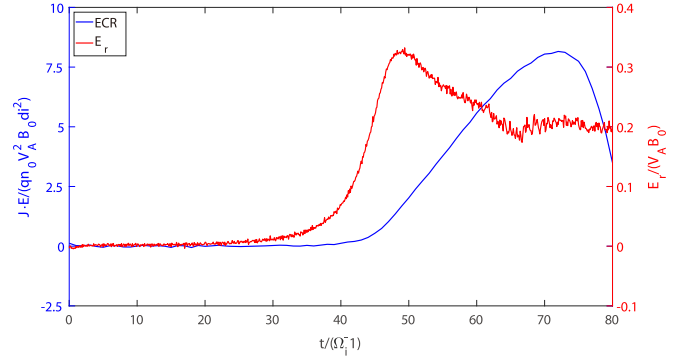


Figure 1. Temporal evolutions of the ECR (blue trace) and the reconnection rate (red trace) in case 1.

$E_r = \partial\Psi/\partial t$, where $\Psi = \max(A_y) - \min(A_y)$ along $Z = 15$ and A_y is the y component of vector potential. The reconnection rate is normalized by $B_0 v_A$. We see that both the reconnection rate and the ECR are nearly zero before $\Omega_i t = 20$. The reconnection rate starts to increase to above 0.3 at around $\Omega_i t = 49$. It then slowly decreases and the reconnection evolves into a quasi-steady stage with a reconnection rate around 0.2 after $\Omega_i t = 65$. On the other hand, the ECR starts to increase at $\Omega_i t = 40$ and reaches maximum at $\Omega_i t = 73$ when the reconnection is already in the quasi-steady stage. Then the ECR decreases until the end of the simulation. The decrease of the ECR is due to the fact that the two reconnection outflows encounter each other as a result of the periodic boundary condition used in our simulation. Obviously, there is a significant time delay, about $24 \Omega_i^{-1}$, between the peak of reconnection rate and the peak of ECR, and $20 \Omega_i^{-1}$ between the onset of the rapid increase of the reconnection rate and the ECR.

Figure 2(a) shows the overview of energy conversion $J \cdot E$ at $\Omega_i t = 52$ when the reconnection fronts (RFs) have fully developed. As the reconnection progresses, the magnetic fields pileup in the outflow region, leading to the rise of magnetic field B_z , which forms the RFs moving away from the X-line (Sitnov et al. 2009; Wu & Shay 2012). We see that the energy conversion at the fronts is stronger than that in the other regions. This agrees with previous observations in the magnetotail (Angelopoulos et al. 2013; Khotyaintsev et al. 2017) and numerical simulations (Sitnov et al. 2009).

Figure 2(d) displays the temporal evolution of the integrated ECR in the whole simulation region, at the fronts and at the X-line, respectively. We see that the energy conversion at the fronts dominates over the other regions. More than two-thirds of the energy conversion occurs at the fronts while the conversion at the X-line is almost negligible. The rest of the energy conversion takes place around the separatrices, as is shown in Figure 2(a). The asynchrony between the reconnection rate and the ECR is due to that the energy conversion predominantly occurs at the RFs rather than at the X-line. Because the buildup of the current and electric field around the RFs is the consequence of reconnection and falls behind the fast rise of the reconnection rate, the temporal evolution of ECR is asynchronized with that of the reconnection rate.

Figures 2(b) and (c) display the energy conversion to ions $J_i \cdot E$ and to electrons $J_e \cdot E$ in the X - Z plane at $\Omega_i t = 52$, respectively. The largest $J_i \cdot E$ is concentrated at the RFs, while $J_e \cdot E$ is the largest at the X-line and the separatrices. It is noticeable that $J_e \cdot E$ has negative values around the RFs, while

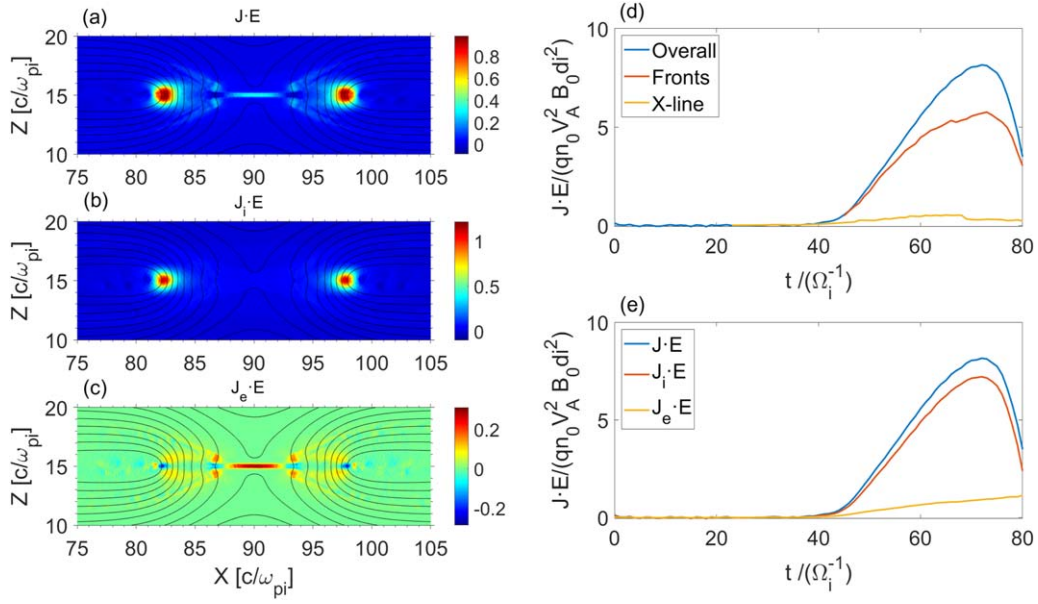


Figure 2. Overview of the energy conversion: (a) $J \cdot E$, (b) $J_i \cdot E$, and (c) $J_e \cdot E$ at $\Omega t = 52$; (d) the overall ECR, the ECR at the RFs and at the X-line as a function of time; (e) the overall $J \cdot E$, $J_i \cdot E$, and $J_e \cdot E$ as a function of time.

it is positive at the X-line, implying that electrons are mainly accelerated by reconnection electric field at the X-line. We integrate $J_i \cdot E$ and $J_e \cdot E$ over the entire simulation region and present their temporal evolution in Figure 2(e). It shows that the magnetic energy mainly goes to ions as $J_i \cdot E$ is the main contribution to the overall energy conversion. About six-sevenths of the released magnetic energy is converted to ions and one-seventh is converted to electrons. One notable feature is that both $J \cdot E$ and $J_i \cdot E$ reach peak at around $\Omega t = 73$ and then drop until the end of the simulation, whereas $J_e \cdot E$ continues to increase slowly after $\Omega t = 73$.

The nonzero $J_i \cdot E$ implies the existence of non-MHD electric field ($E + v_i \times B \neq 0$) at the front. Since $E_y \approx -(v_i \times B)_y$ and $E_z = 0$, the non-MHD electric field must arise from E_x , which deviates from $-(v_i \times B)_x$. It has already been shown that large-amplitude Hall electric field along the front normal existed at RFs (Zhou et al. 2009; Fu et al. 2012). Electric field E_y at the fronts is the ion convective electric field $1/c(u_{ix}B_z - u_{iz}B_x)$, which is related to the transport of magnetic flux associated with the RFs (Zhou et al. 2013), while the reconnection electric field E_y at the X-line is contributed by the off-diagonal electron pressure tensor term (Hesse et al. 1998; Lu et al. 2013). The motional electric field at the RFs is much smaller than the reconnection electric field at the X-line in the early stage of the reconnection (Lu et al. 2013). We also find that the current density J_y at the RFs is much smaller than that at the X-line in the early stage of the reconnection. Therefore, the ECR increases much later than the reconnection rate does.

3.2. Dependence of ECR on the Initial Parameters

In the following we examine the dependence of ECR on the initial parameters of simulation. This provides us with important clues for understanding how the ECR varies in different environments and the underlying physics related to energy conversion during reconnection.

3.2.1. Dependence on the Inflow Density

Figures 3(a) and (b) show the temporal evolution of the reconnection rate and the ECR for different inflow densities, corresponding to cases 2, 3, 4, and 5. A secondary island is formed at $\Omega t = 26$ in case 2 ($n_b/n_0 = 0.04$) and at $\Omega t = 29$ in case 3 ($n_b/n_0 = 0.2$), which leads to the sudden enhancement of the reconnection rate at $\Omega t = 26$ in case 2 and $\Omega t = 29$ in case 3, respectively. This is similar to the result in Karimabadi et al. (2007), which suggests that the formation of secondary islands modulates the reconnection rate. The reconnection rate reaches its maximum value at $\Omega t = 16$ and the ECR reaches maximum at $\Omega t = 27$ in case 2. The reconnection rate reaches maximum at $\Omega t = 32$ and the ECR reaches maximum at $\Omega t = 55$ in case 5 with a larger inflow density of $n_b = n_0$.

It is shown that both the reconnection rate and the conversion rate change drastically with the variation of the inflow density n_b . Reconnection is much faster in the cases with lower inflow density, which is consistent with previous simulations (Wu et al. 2011; Lu et al. 2019). For example, the maximum reconnection rate is about 0.7 in case 2 and is about 0.05 in case 5. The saturated reconnection rate is also larger in cases with lower inflow density.

Below we analyze the dependence of ECR on the inflow density based on a dimensionless analysis of reconnection rate by Wu et al. (2011), which derives a relation $E_r \sim (\delta/L)B_{in}v_{A,in} \sim B_{in}^2/n_{in}^{1/2}$, here B_{in} is the magnetic field in the inflow region, n_{in} is the inflow plasma density and the aspect ratio of the diffusion region δ/L is a constant. We have found in our simulations that $J \cdot E$ is mainly contributed by ion current J_{iy} and electric field E_y at the RFs. According to Ampere's law and the generalized Ohm's law, we find $J_{iy,RF} \sim \partial B_z / \partial x$ and $E_{y,RF} \sim v_{xi}B_z \sim v_{i,out}B_z$. Considering that the RF is an ion-scale structure, the ECR $J \cdot E \sim J_i \cdot E \sim J_{iy,RF}E_{y,RF} \sim v_{i,out}\partial B_z^2 / \partial x \sim v_{i,out}B_z^2/d_i \sim v_{i,out}B_z^2$. The magnetic field at the front scales as $B_z \sim B_{DF} \sim 0.3B_{in}(n_0/n_{in})^{1/2} \sim 0.3v_{A,in}n_0^{1/2}$ as shown in Wu & Shay (2012), here n_0 is the initial plasma sheet density, while the ion outflow speed scales as $v_{i,out} \sim v_{A,in} \sim (B_{in}^2/n_{in})^{1/2}$.

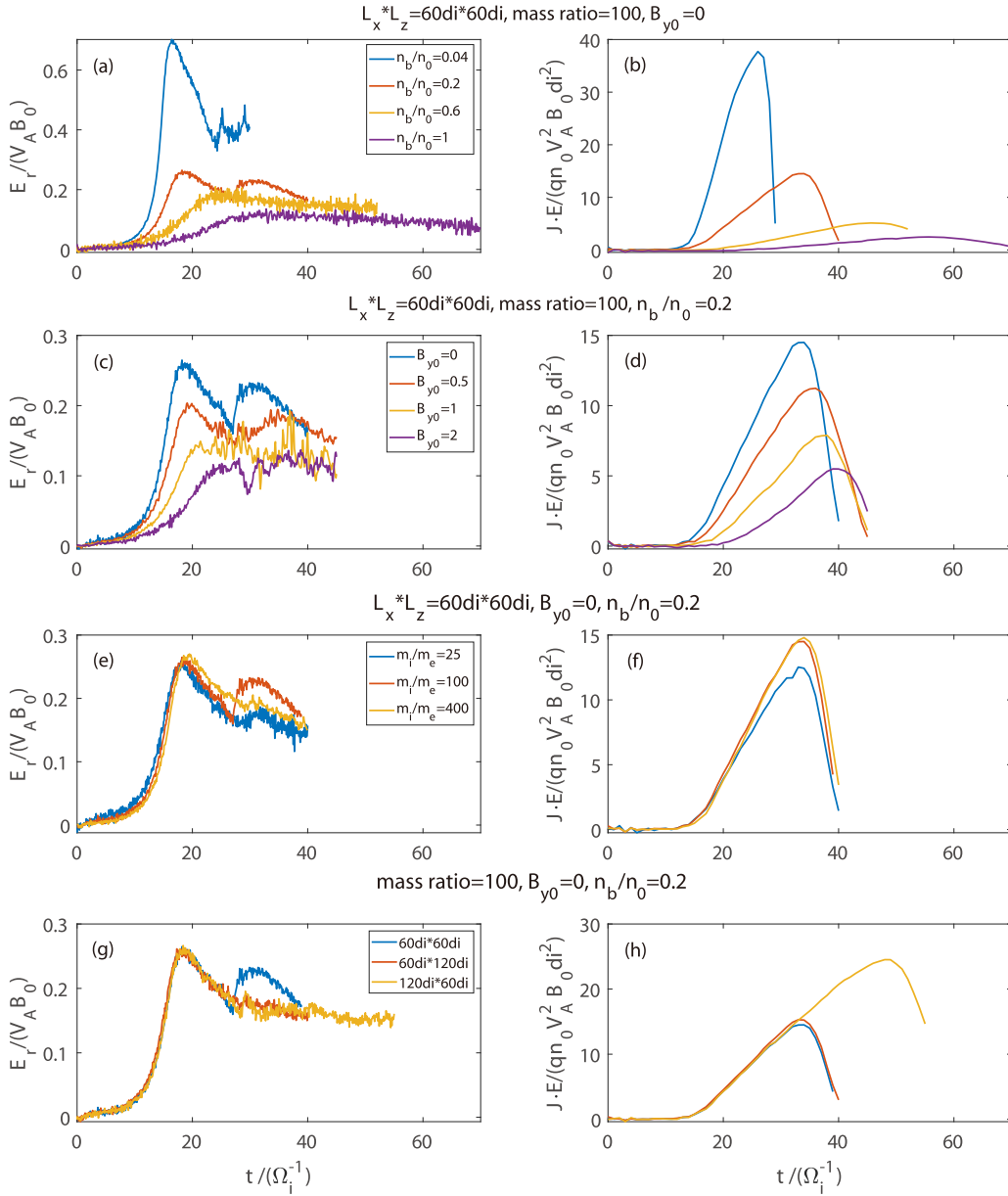


Figure 3. Dependence of the reconnection rate (left column) and the ECR (right column) on the initial parameters of the simulation: (a) and (b) for inflow plasma density; (c) and (d) for guide field; (e) and (f) for mass ratio; and (g) and (h) for simulation size.

(Wu et al. 2011). Combining the equations above, we get $J \cdot E \sim v_{i,\text{out}} B_z^2 \sim B_{\text{DF}}^2 v_{A,\text{in}} \sim v_{A,\text{in}}^3 n_0$. As demonstrated in Wu et al. (2011), the decrease of n_{in} leads to an increase of $v_{A,\text{in}}$ and the reconnection rate (Wu et al. 2011). Since n_0 is a constant, the decrease of n_{in} results in the increases of the ECR.

3.2.2. Dependence on the Guide Field

It has been shown that the presence of a guide field substantially modifies the particle dynamics and the geometry of reconnection (Pritchett 2001; Ricci et al. 2004; Fu et al. 2006; Huang et al. 2010; Zhou et al. 2019). Here we examine the effects of a guide field on the ECR. Figures 3(c) and (d) show the time evolution of the reconnection rate and the ECR in cases 3, 6, 7, and 8. Secondary magnetic islands are generated in these cases because the guide field facilitates the extension of the current layer and makes tearing instability unstable (Drake et al. 2006). Similar to cases 2 and 3, the

formation of secondary islands results in the enhancements of the reconnection rate. However, there are no corresponding enhancements in the ECRs in these cases. The reconnection rate reaches its peak at $\Omega_i t = 19$ and the ECR reaches its peak at $\Omega_i t = 34$ in case 3 without a guide field. The reconnection rate reaches its peak at $\Omega_i t = 28$ and the ECR reaches peak at $\Omega_i t = 40$ in case 8 with large guide field $B_{y0} = 2$. It seems that the guide field postpones the encounter of the two outflows, which is probably due to the fact that the reconnection outflows are weaker in the presence of a larger guide field.

We see that both the reconnection rate and the ECR are largely affected by the guide field. The peak reconnection rate is larger in the cases with smaller guide fields. It is suggested that $J \times B$ force associated with the Hall term reduces the inflow velocity due to the presence of the guide field, and hence reduces the reconnection rate (Huba 2005; Tharp et al. 2013). The saturated reconnection rate, i.e., the reconnection rate in

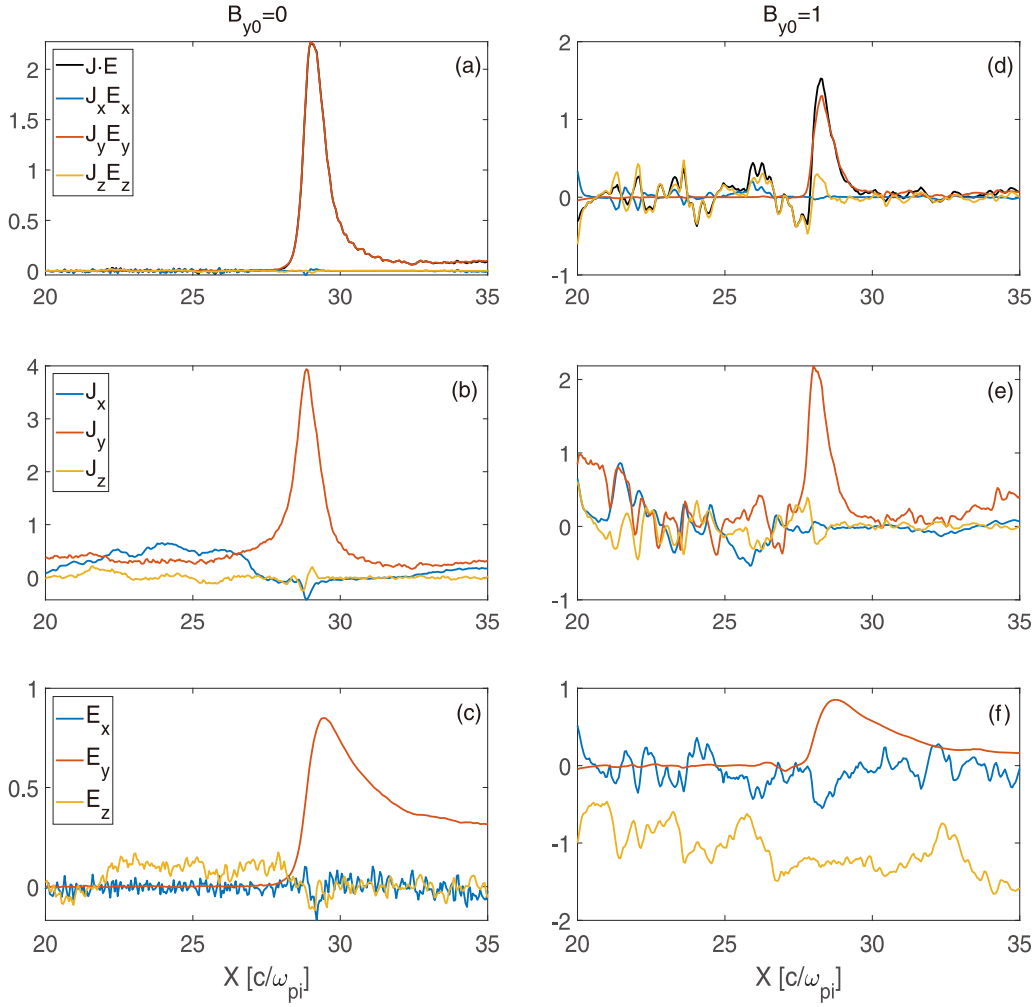


Figure 4. Comparison of $J \cdot E$, current densities and electric fields between case 3 without a guide field (left column) and case 7 with a guide field $B_{y0} = 1$ (right column). Panels (a) and (d): the three components of $J \cdot E$, $J_x E_x$, $J_y E_y$, $J_z E_z$, and the $J \cdot E$. Panels (b) and (e): the three components of the current density. Panels (c) and (f): the three components of the electric field. All of these values are obtained along the line of $Z = 15$.

the quasi-steady phase, however, does not differ substantially among these cases. Even in the case with $B_{y0} = 2B_0$, the saturated reconnection rate is about 0.1. This agrees with previous simulations that fast reconnection is achieved in the large guide field regime (Ricci et al. 2004; Swisdak et al. 2005; Liu et al. 2015). The peak ECR decreases as the increment of the guide field.

Since the energy conversion in guide field reconnection also takes place predominantly at RFs, we focus on the energy conversion at the RFs in order to understand why the ECR is reduced in guide field reconnection. Figure 4 compares $J \cdot E$ at the RF on the $+X$ side of the X-line between case 3 ($B_{y0} = 0$) and case 7 ($B_{y0} = 1$). The three components of electric field and current are also compared. In the case without guide field, $J \cdot E$ is dominated by $J_y E_y$ at the RF. The large J_y at the RF is due to the accumulation of plasmas at RF and ion acceleration by the electric field E_y . Current J_x and J_z do not contribute to $J \cdot E$ at the RF (Figure 4(a)) since J_x and J_z are nearly 0 (Figure 4(b)), and E_x and E_z are much smaller than E_y (Figure 4(c)).

In the guide field case, $J_y E_y$ drops and there is a bipolar variation of $J_z E_z$ near the RFs because of a bipolar current J_z and a large negative Hall electric field E_z (as shown in Figures 4(d)–(f)). The guide field causes additional components

of the $E \times B$ drift, which modifies the flow pattern in the X – Z plane and results in asymmetric plasma flow with respect to the X-line (Ricci et al. 2004). A strong electric field E_z and additional current J_z emerges at the RF in the guide field reconnection. However, $J \cdot E$ is still dominated by $J_y E_y$, similar to the zero-guide field case. Figure 5(a) shows that the magnetic field B_z in the case without a guide field is larger than that in the guide field case, whereas the ion outflow velocity v_{ix} is smaller in the case without a guide field (Figure 5(b)). $v_{ix} B_z^2$ is larger in the case without a guide field than the guide field case (Figure 5(c)). Since $J \cdot E$ is proportional to $v_{i,\text{out}} B_z^2 \sim v_{ix} B_z^2$, as we have discussed in Section 3.2.1, the ECR is reduced in the guide field case.

3.2.3. Dependence on the Mass Ratio

Figures 3(e) and (f) show the time evolution of the reconnection rate and the ECR in cases 3, 9, and 10, which employ different mass ratios. The reconnection rate differs little in different cases, except that the reconnection rate in case 3 ($m_i/m_e = 100$) exhibits an obvious enhancement at about $\Omega_e t = 26$ because of the generation of a secondary magnetic island. Similar to the reconnection rate, the mass ratio neither changes the peak value of the ECR, nor affects the peak time of the ECR, as is demonstrated in Figure 4(f).

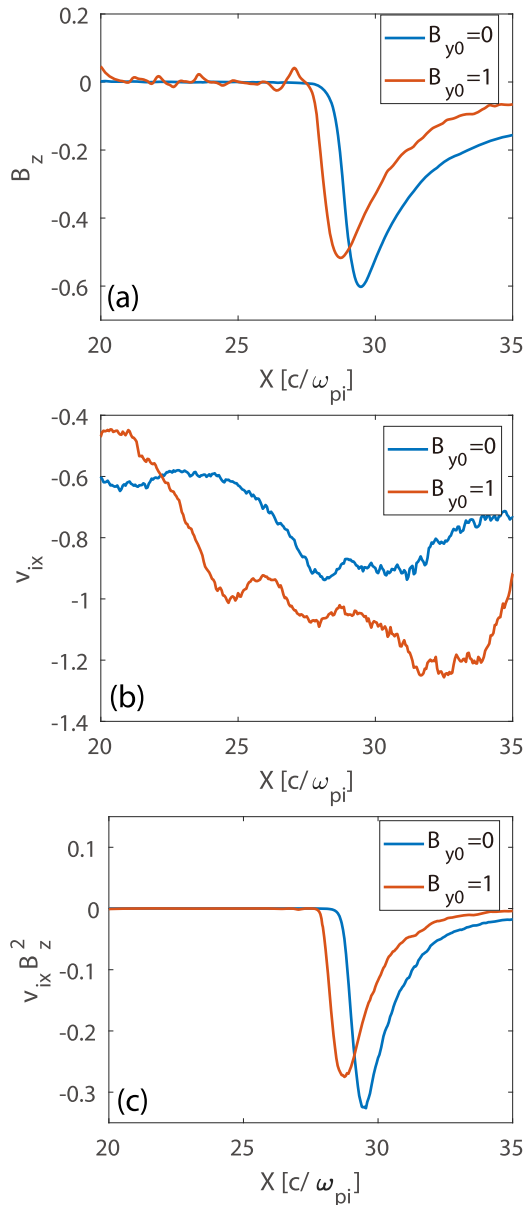


Figure 5. Comparison between case 3 (blue trace) and case 7 (red trace). (a) The magnetic field B_z ; (b) the ion outflow velocity v_{ix} , and (c) $v_{ix} B_z^2$. These values are obtained along $Z = 15$ and at the time when the ECR reaches its peak in each simulation.

The independence of the reconnection rate on the mass ratio implies that the reconnection rate is irrelevant to the mechanism breaking the field lines in the electron diffusion region (Hesse & Winske 1998; Shay & Drake 1998). The fact that the ECR is independent of the mass ratio is consistent with our results that the magnetic energy mainly goes to ions and the ECR is predominantly contributed by $J_i \cdot E$. It also implies that electron physics is unimportant in determining the ECR.

4. Discussion and Conclusions

We have mentioned that the decrease of ECR in these simulations is due to the periodic boundary in the outflow direction, thus it is interesting to know whether the peak ECR is larger in a simulation with a larger simulation region. Figures 3(g) and (h) display the reconnection rate and ECR as functions of time for different simulation sizes in cases 3, 11,

and 12. The reconnection rates in these cases are similar, except that they have an enhancement in case 3 ($60d_i \times 60d_i$) because of the generation of a secondary magnetic island. The ECRs are almost the same among these three cases before $\Omega_i t = 34$. Then the ECR reaches peak and decreases after $\Omega_i t = 34$ in cases 3 and 11, whereas the ECR continues to increase until $\Omega_i t = 49$ in case 12, which has a longer simulation region.

The peak value of ECR in case 12 is about twice that in cases 3 and 11, in which the length along the outflow direction is half of that in case 12. On the other hand, enlarging the size in the Z direction does not change the ECR. The two outflows encounter each other much later as a result of a larger size in the X direction. Thus, the magnetic flux has more time to accumulate, which leads to stronger B_z around the RF in the outflow region. Moreover, a longer simulation region may produce larger energy conversion regions. These combined effects probably cause the larger ECR in case 12 with a longer outflow region. However, the change in the Z direction does not affect the time of flow encounter and hence does not affect the ECR. A critical question is whether the peak ECR has an upper limit if the outflow region is infinitely long. This question can be addressed in the future by performing a simulation with an open boundary or extremely large region.

Secondary magnetic islands are easier to be produced in the presence of a guide field and low inflow density (Wang et al. 1988; Wan & Lapenta 2008; Lu et al. 2019). Although it has been illustrated that secondary islands are closely related to electron energization (Drake et al. 2006; Wang et al. 2010, 2017; Huang et al. 2014; Zhou et al. 2018), we notice that the formation of secondary islands does not affect the ECR. Our simulation only produces one single secondary island in each case, hence we do not know whether the ECR can be influenced by the formation of multiple secondary islands. If multiple islands are produced in the system, they may coalesce to form a larger island, which probably affects the overall ECR in the system since coalescence is associated with significant energy dissipation (Zhou et al. 2014, 2017b; Wang et al. 2016a, 2016b). The role of secondary islands in energy conversion in multiple X-line reconnection is outside the scope of this study and will be discussed in the future.

Using 2.5D PIC simulations, we illustrate that the reconnection rate is not synchronized to the ECR because the magnetic energy conversion predominantly occurs at the RFs rather than at the X-line. Our results show that the dependence of ECR on the inflow plasma density, guide field and mass ratio is similar to that of the reconnection rate. With the increase of the inflow density, both the reconnection rate and the ECR decreases. The presence of a guide field leads to the reduction of both the reconnection rate and the ECR, though reconnection remains fast. Furthermore, the ECR is independent of the ion–electron mass ratio because the electromagnetic energy is mainly converted to ions. However, the ECR is sensitive to the length of the simulation region in the outflow direction. Although the decrease of the ECR in our simulation is caused by flows encountered due to the periodic boundary condition, this phenomenon is relevant to multiple X-line reconnection, where the outflows may encounter each other in a magnetic island as this is the natural consequence of multiple X line reconnection (Øieroset et al. 2011). The energy conversion in multiple X-line reconnection will be the subject of our future study.

This work is supported by the National Natural Science Foundation of China (NSFC) under grant 41774154 and Jiangxi Provincial Graduate Innovation Special Fund Project under grant YC2019-S047. The PIC simulations were performed by using the TH-1A supercomputer at Tianjin (nssc-tj) and the TH-2 supercomputer at Guangzhou (nssc-gz).

ORCID iDs

Yongyuan Yi  <https://orcid.org/0000-0002-0594-8031>
Liangjin Song  <https://orcid.org/0000-0003-3934-2094>

References

- Angelopoulos, V., Runov, A., Zhou, X. Z., et al. 2013, *Sci*, 341, 1478
Birn, J., Drake, J. F., Shay, M. A., et al. 2001, *JGR*, 106, 3715
Biskamp, D. 1986, *PhFl*, 29, 1520
Chen, P. F., & Shibata, K. 2000, *ApJ*, 545, 524
Deng, X. H., & Matsumoto, H. 2001, *Natur*, 410, 557
Drake, J. F., Swisdak, M., Che, H., et al. 2006, *Natur*, 443, 553
Fu, H. S., Khotyaintsev, Y. V., Vaivads, A., et al. 2012, *GeoRL*, 39, L06105
Fu, X. R., Lu, Q. M., & Wang, S. 2006, *PhPI*, 13, 012309
Hesse, M., & Winske, D. 1998, *JGR*, 103, 26479
Huang, C., Lu, Q., & Wang, S. 2010, *PhPI*, 17, 072306
Huang, S. Y., Fu, H. S., Yuan, Z. G., et al. 2015, *JGRA*, 120, 4496
Huang, S. Y., Zhou, M., Yuan, Z. G., et al. 2014, *JGRA*, 119, 7402
Huba, J. D. 2005, *PhPI*, 12, 012322
Karimabadi, H., Daughton, W., & Scudder, J. 2007, *GeoRL*, 34, L13104
Khotyaintsev, Y. V., Divin, A., Vaivads, A., et al. 2017, *GeoRL*, 44, 1234
Kulsrud, R. M. 2001, *EP&S*, 53, 417
Lapenta, G., Goldman, M., Newman, D., et al. 2014, *PhPI*, 21, 055702
Liu, Y. H., Guo, F., Daughton, W., et al. 2015, *PhRvL*, 114, 095002
Liu, Y. H., Hesse, M., Guo, F., et al. 2017, *PhRvL*, 118, 085101
Lu, Q., Lu, S., Huang, C., et al. 2013, *PPCF*, 55, 085019
Lu, Q., Wang, H., Huang, K., et al. 2018, *PhPI*, 25, 072126
Lu, S., Artemyev, A. V., Angelopoulos, V., et al. 2019, *GeoRL*, 46, 28
Øieroset, M., Phan, T. D., Eastwood, J. P., et al. 2011, *PhRvL*, 107, 165007
Parker, E. 1957, *PhRv*, 107, 830
Petschek, H. E. 1964, *NASSP*, 50, 425
Pritchett, P. L. 2001, *JGR*, 106, 3783
Ricci, P., Brackbill, J. U., Daughton, W., et al. 2004, *PhPI*, 11, 4102
Russell, C. T., & McPherron, R. L. 1973, *SSRv*, 15, 205
Shay, M. A., & Drake, J. F. 1998, *GeoRL*, 25, 3759
Shay, M. A., Drake, J. F., Rogers, B. N., et al. 1999, *GeoRL*, 26, 2163
Sitnov, M. I., Merkin, V. G., Swisdak, M., et al. 2014, *JGRA*, 119, 7151
Sitnov, M. I., Swisdak, M., & Divin, A. V. 2009, *JGRA*, 114, A04202
Sweet, P. A. 1958, in *IAU Symp. 6, Electromagnetic Phenomena in Ionized Gases*, ed. B. Lehnert (Cambridge: Cambridge Univ. Press), 123
Swisdak, M., Drake, J. F., Shay, M. A., et al. 2005, *JGRA*, 110, A05210
Tharp, T. D., Yamada, M., Ji, H., et al. 2013, *PhPI*, 20, 055705
Wan, W., & Lapenta, G. 2008, *PhRvL*, 101, 015001
Wang, H., Lu, Q., Huang, C., et al. 2016a, *ApJ*, 821, 84
Wang, H., Lu, Q., Huang, C., et al. 2017, *PhPI*, 24, 052113
Wang, R., Lu, Q., Du, A., et al. 2010, *PhRvL*, 104, 175003
Wang, R., Lu, Q., Nakamura, R., et al. 2016b, *NatPh*, 12, 263
Wang, S., Lee, L. C., & Wei, C. Q. 1988, *PhFl*, 31, 1544
Wu, P., & Shay, M. A. 2012, *GeoRL*, 39, L08107
Wu, P., Shay, M. A., Phan, T. D., et al. 2011, *PhPI*, 18, 111204
Yamada, M., Yoo, J., Jara-Almonte, J., et al. 2014, *NatCo*, 5, 4774
Zhou, M., Ashour-Abdalla, M., Deng, X., et al. 2009, *GeoRL*, 36, L20107
Zhou, M., Ashour-Abdalla, M., Deng, X., et al. 2017a, *JGRA*, 122, 9513
Zhou, M., Berchem, J., Walker, R. J., et al. 2017b, *PhRvL*, 119, 055101
Zhou, M., Deng, X., Ashour-Abdalla, M., et al. 2013, *JGRA*, 118, 674
Zhou, M., Deng, X. H., & Huang, S. Y. 2012a, *PhPI*, 19, 042902
Zhou, M., Deng, X. H., Pang, Y., et al. 2012b, *PhPI*, 19, 072907
Zhou, M., Deng, X. H., Zhong, Z. H., et al. 2019, *ApJ*, 870, 34
Zhou, M., El-Alaoui, M., Lapenta, G., et al. 2018, *JGRA*, 123, 8087
Zhou, M., Pang, Y., Deng, X., et al. 2014, *JGRA*, 119, 6177
Zhou, M., Pang, Y., Deng, X. H., et al. 2011, *JGRA*, 116, A06222